Nanoscale Advances

ROYAL SOCIETY OF CHEMISTRY

PAPER

View Article Online
View Journal | View Issue

Open Access Article. Published on 10 September 2025. Downloaded on 1/22/2026 1:25:36 PM.
This article is licensed under a Creative Commons Attribution-NonCommercial 3.0 Unported Licence.

Check for updates

Cite this: *Nanoscale Adv.*, 2025, **7**, 6851

A stepwise responsive Au-SS-PEG/Sor/ATP$_{aptamer}$/LHRH-MPG$^{\Delta NLS}$ drug delivery vector system for overcoming drug resistance in immunotherapy of hepatocellular carcinoma

Mengting Tong,[a] Guangpeng Chen,[b] Yong Dong,[b] Yubin Pan,[b] Yanan Xue[b] and Da Li *[b]

Received 14th January 2025
Accepted 16th August 2025

DOI: 10.1039/d5na00056d

rsc.li/nanoscale-advances

Despite the progress made in novel immunotherapy for hepatocellular carcinoma (HCC), drug resistance remains a challenging problem. In this study, we developed a stepwise nanodrug delivery system, known as Au-SS-PEG/Sor/ATP$_{aptamer}$/LHRH-MPG$^{\Delta NLS}$, to adapt to the high concentrations of glutathione (GSH) and adenine nucleoside triphosphate/adenosines (ATP/ADO) found in cancer cells and the tumor microenvironment (TME). This system utilizes novel Au nanoclusters conjugated with disulfide-linked PEG as vectors to transport sorafenib (Sor) and an ATP-binding nucleic acid aptamer (ATP$_{apt}$). It can enter HCC cells through luteinizing hormone-releasing hormone (LHRH)-MPG$^{\Delta NLS}$ (LM). Within the cells, the disulfide bonds of the nanoclusters are cleaved by the high levels of GSH, leading to the release of Sor/ATPapt. This release can be further triggered by ATP/ADO, resulting in a stepwise drug release mechanism. Furthermore, this nanodrug system has exhibited the ability to overcome αPD-1 resistance in HCC tumors. In summary, our novel drug delivery system demonstrates a dramatic anti-HCC effect and holds great potential for treating HCC patients.

1 Introduction

HCC is one of the most common cancers and a leading culprit of cancer-related death worldwide.[1] Despite the availability of novel drugs and therapies, such as immunotherapy based on PD-1/PD-L1 inhibitors,[2] the treatment of HCC remains challenging due to drug resistance,[3] leading to a poor prognosis for HCC patients.

The mechanisms underlying drug resistance in HCC patients are diverse.[4] Among them, ATP is instrumental in the development of drug resistance. For instance, high levels of ATP in HCC cells can intensify the activity of the multidrug-resistant protein ABCG2.[5] In addition, the high concentration of ATP in the TME, resulting from the growth and cell death of cancer cells, could be metabolized to ADOs by CD39 and CD73.[6] ADOs are potent immunosuppressive factors that hinder the effectiveness of immunotherapy.[7] Therefore, drugs targeting ADO-related genes, such as anti-CD39 antibodies, anti-CD73 antibodies, and A2AR inhibitors, have been developed to overcome drug resistance.[8–11]

However, achieving efficient and precise targeted delivery of anti-cancer drugs *in vivo* remains a challenge.[12,13] For example, drugs are susceptible to clearance by the reticuloendothelial system during blood circulation and can be hindered by the high tumor interstitial pressure from penetrating deep into tumors.[14,15] Consequently, there is an urgent need to develop novel drug delivery systems that can foster drug release within cancer cells, thereby refining cancer treatment.

The luteinizing hormone-releasing hormone (LHRH) receptor is highly expressed in breast, ovarian, and prostate cancer cells.[16,17] LHRH is overexpressed in HCC cells[18,19] but is not expressed in most visceral organs,[20] making the LHRH peptide a valuable targeting component in drug delivery systems as it facilitates drug uptake by LHRH-expressing cells.[21–23] Moreover, cancer cells produce dramatic amounts of glutathione (GSH),[24] so considerable efforts have been made to develop nanodrug delivery systems for cancer treatment based on GSH.[25–27]

Gold (Au) nanoparticles have gained extensive attention due to their good biocompatibility, low cytotoxicity, abundant surface-active sites suitable for surface modification, and responsive properties.[28,29] Enhancing the physical and chemical properties of Au nanoparticles, such as linking them with disulfide bonds, is a promising approach to creating intelligent and responsive drug delivery systems.[30,31] For example, Feng *et al.*[32] synthesized a nanodrug delivery system, DOX-EGF-SA-Au

[a]*Second Department of Medical Oncology, The Fourth Affiliated Hospital of Xinjiang Medical University, Urumqi, Xinjiang, China*

[b]*Department of Medical Oncology, Sir Run Run Shaw Hospital, Zhejiang University School of Medicine, Hangzhou, Zhejiang, China. E-mail: lidaonconew@zju.edu.cn; Tel: +86-13656710929*

Open Access Article. Published on 10 September 2025. Downloaded on 1/22/2026 1:25:36 PM.
This article is licensed under a Creative Commons Attribution-NonCommercial 3.0 Unported Licence.

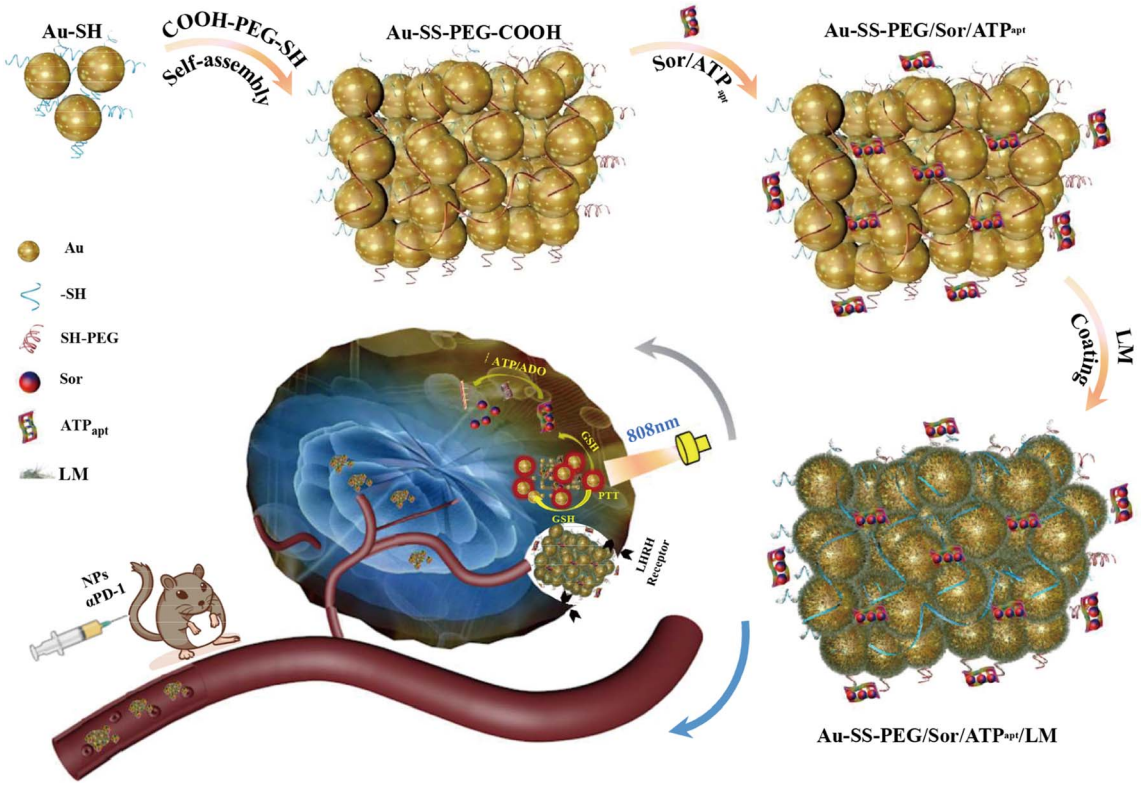

Scheme 1 Preparation pipeline and anti-cancer mechanism of Au-SS-PEG/Sor/ATP_{apt}/LM nanoclusters.

NPs, to treat brain tumors. Zhao *et al.*[33] achieved nanodrugs with excellent GSH and NIR responsiveness by modifying the surface of hollow mesoporous carbon (HMC). They loaded HMC with DOX, introduced Au–S bonds, and sealed the ends with polyethylene glycol.

In this project, we developed a stepwise drug release system using Au nanoclusters linked with disulfide-PEG, the anti-HCC drug Sor, ATP_{apt}, and LM (Scheme 1). This system was designed to adapt to the high concentrations of GSH and ATP-ADO in HCC cells and the TME, cleaving the disulfide bonds to release Sor/ATP_{apt}, which was further dissociated by ATP/ADO, resulting in a stepwise drug release. We also evaluated the anti-cancer efficacy of this system in HCC cells and HCC tumors, particularly in αPD-1-resistant HCC tumors.

2 Experiments

2.1 Chemicals

All the chemical reagents were analytically pure. 2,2′-Dithiodipyridine ($C_{10}H_8N_2S_2$), 1-(3-dimethylaminopropyl)-3-ethylcarbodiimide hydrochloride (EDC), *N*-hydroxysuccinimide (NHS), sodium citrate ($Na_3C_6H_5O_7 \cdot 2H_2O$) and Sor were purchased from Shanghai Aladdin Bio-Chem Technology (Shanghai, China). Chloroform ($CHCl_3$) and methanol (CH_3OH) were provided by Sinopharm Chemical Reagent (Shanghai, China). Chloroauric acid ($HAuCl_4$) was obtained from Shanghai Macklin Biochemical (Shanghai, China). Carboxyl polyethylene glycol sulfhydryl (COOH-PEG-SH, M.W. 2000) and polyethylene glycol sulfhydryl (HS-PEG-SH, M.W. 2000) were from Shanghai Pengsheng Biological (Shanghai, China). Aptamer (ATP_{apt}, 5′-amination modification), complementary DNA (cDNA) (5′-ACC TTC CTC CGC AAT ACT CCC CCA GGT-3′), and GSH were bought from Shanghai Sangon Bioengineering Technology (Shanghai, China). LM was purchased from Shanghai Peptides Biotechnology (Shanghai, China). PD-1 inhibitor (αPD-1) was obtained from Sir Run Run Shaw Hospital, Zhejiang University School of Medicine (Hangzhou, Zhejiang, China). A ready-to-use dialysis bag 54-3500D RC membrane (MW: 3500D) was provided by Zhejiang Life Science Biotechnology (Hangzhou, Zhejiang, China).

2.2 Establishment of the nanodrug delivery system

The procedures entailed four sequential steps: preparation of Au-SH nanospheres, self-assembly of Au-SH nanospheres to Au-SS-PEG nanoclusters, loading ATP_{apt} onto Au-SS-PEG/Sor, and coating of Au-SS-PEG/Sor/ATP_{apt} with LM.

2.2.1 Preparation of Au-SH nanospheres. Au-SH nanospheres were prepared by utilizing two different pipelines as

Table 1 Au-SH preparation pipelines

Pipeline	1% wt $HAuCl_4$ (μL)	1% Sodium citrate (mL)
1	1000	20
2	58.6	10

 © 2025 The Author(s). Published by the Royal Society of Chemistry

Open Access Article. Published on 10 September 2025. Downloaded on 1/22/2026 1:25:36 PM. This article is licensed under a Creative Commons Attribution-NonCommercial 3.0 Unported Licence.

described in Table 1. In the first pipeline, 1000 μL of 1% wt chloroauric acid was introduced into 100 mL of deionized water, which was then gradually heated to 100 °C with continuous stirring. When the solution reached a boiling point, 20 mL of 1% wt sodium citrate solution was rapidly introduced. Once the solution turned deep red, the heater was turned off, allowing it to slowly cool down to room temperature (RT). Subsequently, 1 mL of HS-PEG-SH solution, containing 600 μg HS-PEG-SH, was mixed with the solution at RT with constant stirring for 3 h. Finally, the nanospheres were collected by centrifugation at 10 000 rpm and washed with deionized water. In the second pipeline, 58.6 μL of 1% wt chloroauric acid was added to 100 mL of deionized water, and the subsequent steps were the same as described above.

2.2.2 Preparation of Au-SS-PEG nanoclusters. 50 mg of Au-SH nanospheres were introduced into a 50 mL phosphate buffer saline (PBS) solution and thoroughly dispersed. Next, 50 mg of 2,2′-dithiodipyridine was introduced into the solution, and the mixture was stirred at RT for a duration of 12 h. Following the completion of the reaction, the mixture was subjected to extensive washing with methanol and PBS and then dried in a vacuum at 30 °C. Subsequently, the modified dry nanoparticles were re-dispersed in a 50 mL chloroform solution and subjected to 15 min of sonication. Following sonication, the mixture was incubated with 65 mg of COOH-PEG-SH and stirred at RT for 24 h. After this incubation period, the nanoparticles were collected by centrifuging the reaction mixture at 10 000 rpm for 15 min at 4 °C, washed with a PBS buffer, and re-dispersed in PBS.

2.2.3 Preparation of Au-SS-PEG/Sor/ATP$_{apt}$. First, a mixture of Au-SS-PEG, EDC·HCl, and NHS in a molar ratio of 4 : 3 : 1 was prepared and sonicated for 20 min. Concurrently, equal amounts of 5′-amino modified ATP$_{apt}$ (5′-ACC TGG GGG AGT ATT GCG GAG GAA GGT-3′) and cDNA (5′-ACC TTC CTC CGC AAT ACT CCC CCA GGT-3′) were dispersed in PBS. This dispersion was then added to 1 mL of PBS buffer with pH ranging from 4 to 7 at a concentration of 2 mg mL^{-1}, along with Sor. The two mixtures were subsequently combined with continuous stirring for a duration of 24 h. Following the completion of the reaction, the nanoparticles were collected by centrifuging the mixture at 10 000 rpm for 15 min at 4 °C, washed with a PBS buffer, and dried at a low temperature. To confirm whether ATP$_{apt}$ (27 bp) was successfully loaded onto Au-SS-PEG, the nanoclusters underwent DNA gel electrophoresis. Similarly, Cy5.5-NH$_2$ and FITC-NH$_2$ were mixed with ATP$_{apt}$ and cDNA, respectively, and then introduced into the reaction to obtain Cy5.5- and FITC-labeled Au-SS-PEG/Sor/ATP$_{apt}$ and Au-SS-PEG/Sor/ATP$_{apt}$/LM nanoparticles.

2.2.4 Preparation of Au-SS-PEG/Sor/ATP$_{apt}$/LM nanoclusters. Au-SS-PEG/Sor/ATP$_{apt}$ nanoclusters were first resuspended in PBS and activated by the addition of the appropriate amounts of EDC·HCl and NHS. Subsequently, the suspension was mixed with 10 mg of LHRH-MPG$^{\Delta NLS}$ (GRLWYSWHEGALFLGFLGAAGSTMGAWSQ-PKSKRKV) and stirred for a period of 24 h. Following this, the solution was subjected to centrifugation, and the resulting pellet was washed with 2-(*N*-morpholino) ethanesulfonic acid hydrate (MES) buffer. The washed pellet was then dried at a low temperature and subjected to protein gel electrophoresis to confirm the presence of LM in the nanoclusters. For comparison, a protein marker and LM (4.6 kDa) were employed as controls in the gel electrophoresis analysis.

2.3 Material testing and characterization

2.3.1 Morphological analysis. Dynamic light scattering (DLS) was utilized to determine the size of the nanoparticles with a Zetasizer Nano ZS90 (Malvern Panalytical, Worcestershire, UK). A scanning transmission electron microscope (STEM) was employed to observe the morphology of the nanoparticles with a JEM-2100 machine (JEOL, Kyoto, Japan). The chemical structure of gold nanoparticles assembled with PEG and disulfide bonds was detected using a Fourier transform infrared spectrometer (FTIR, Nicolet 6700, Thermo Fisher Scientific, Kansas, USA). The release of Sor was measured using an ultraviolet-visible (UV-Vis) spectrophotometer (UV-3600, Shimadzu, Kyoto, Japan).

2.3.2 Tests for Sor release responding to GSH and/or ATP. 10 mg of Au-SS-PEG/Sor/ATPapt/LM was placed inside a dialysis bag, which was then immersed in a 10 mL release solution consisting of PBS/0.1% Tween-80 (PBST) containing 10 mM GSH and/or ATP. The entire setup was placed on a shaking platform at RT and oscillated for a duration of 24 h. The timing commenced at the start of oscillation, and at predetermined time intervals, 0.5 mL of the release solution was pipetted into an EP tube. Subsequently, PBST solution with an equivalent amount of GSH and/or ATP was added for further release under the same conditions. The concentration of Sor in the supernatant was detected using UV-Vis, with the absorbance value (OD) measured at 260 nm. The relative cumulative release characteristics of Sor were evaluated by utilizing PBST as the control group. Specific experimental conditions are detailed in Table 2.

2.3.3 Influence of nanoclusters on erythrocytes. For the hemolysis test, 0.5 mL of blood was collected from the orbital sinus of each mouse to prepare a 5% erythrocyte suspension, which was then divided into six test tubes, with each containing 2.5 mL of the suspension. Tubes 1 to 4 were sequentially supplemented with 0.4, 0.3, 0.2, and 0.1 mL of the Au-SS-PEG/Sor/ATP$_{apt}$/LM suspension, followed by the addition of saline to reach a total volume of 5 mL. Tube 5 and Tube 6 were filled with saline and distilled water, serving as negative and positive controls, respectively. All samples were incubated at 37 °C for 30 min. Specific parameters are detailed in Table 3. Subsequently, the OD values of the supernatant from each group were measured at 540 nm using a microplate reader, and the hemolysis rate was calculated.

Table 2 Conditions of the tests for Sor release assays

	No.			
Content	1	2	3	4
20 mM GSH	-	+	-	+
20 mM ATP	-	-	+	+

Open Access Article. Published on 10 September 2025. Downloaded on 1/22/2026 1:25:36 PM.
This article is licensed under a Creative Commons Attribution-NonCommercial 3.0 Unported Licence.

Table 3 Setup of hemolysis tests

	Tube (mL)					
Content	1	2	3	4	5	6
5% red blood cells	2.5	2.5	2.5	2.5	2.5	2.5
0.9% NaCl	2.1	2.2	2.3	2.4	2.5	—
Distilled water	—	—	—	—	—	2.5
NP solution	0.4	0.3	0.2	0.1	—	—

For inverted microscopy and TEM inspection, a 5% erythrocyte suspension was introduced to each well of a 12-well cell culture plate (2 mL per well), mixed, and housed in a CO_2 incubator for 1 h. Subsequently, 0.2 mL of Au-SS-PEG/Sor/ATP_{apt}/LM was added to each well and thoroughly mixed. After an additional 1 h incubation at 37 °C, the cells were observed under an inverted microscope. For further examination, the cells were subjected to fixation, dehydration, embedding, and sectioning using an LKB ultra-thin slicer. Finally, the samples were stained, dried, and examined by utilizing a Hitachi H-600A TEM (Tokyo, Japan) from Japan.

2.3.4 Protein gel electrophoresis and plasma adsorption capacity detection. The Au-SS-PEG/Sor/ATP_{apt}/LM suspension was incubated with 30% fetal bovine serum (FBS, Gibco, Tulsa, Oklahoma, USA). The particle size of the Au-SS-PEG/Sor/ATP_{apt}/LM nanoclusters was assessed both before and after this incubation using a nanoparticle size analyzer. Following the incubation, the nanoclusters were pelleted by centrifugation, and their anti-protein adsorption performance was evaluated by utilizing SDS-PAGE. For comparison, FBS, Au, AU-SH, and Au-SS-PEG were included as control samples.

2.3.5 Photothermal performance test. The photothermal conversion performance of the Au-SS-PEG/Sor/ATP_{apt}/LM nanoclusters was assessed with the use of an infrared thermal imager (HIKVISION, Hangzhou, Zhejiang, China). In this evaluation, an appropriate amount of Au-SS-PEG/Sor/ATP_{apt}/LM nanoclusters was resuspended in 2 mL of PBS buffer and subjected to irradiation with near-infrared (NIR) rays at 808 nm and an intensity of 2 W cm^{-2} for 10 min. Simultaneously, a PBS solution was employed as a blank control group. A thermal imager was utilized to measure the rate of temperature change in the solution per minute, and a curve illustrating the temperature changes throughout the illumination was plotted.

2.4 Cell experiments

2.4.1 Cell uptake assay. Human hepatocyte LO2 cells, HCC cells HepG2, and mouse HCC cells H22 were purchased from the National Collection of Authenticated Cell Cultures (China) and maintained in RPMI-1640 medium containing 10% FBS and 100 U mL^{-1} penicillin/streptomycin (Cytiva, Logan, Utah, USA) in a 37 °C incubator supplied with 5% CO_2.

The cellular uptake of Au-SS-PEG/Sor/ATP_{apt} before and after LM coating was analyzed. HepG2 cells were inoculated into 6-well plates with a density of 5×10^4 cells per mL and cultured overnight. Then Au-SS-PEG/Sor/ATP_{apt}/LM and Au-SS-PEG/Sor/ATP_{apt} conjugated with FITC were incubated with the indicated cells, followed by washing with PBS. Finally, the cells were stained with 200 μL DAPI and observed using a laser scanning confocal microscope (Leica, Wetzlar, Germany).

2.4.2 CCK-8 cell viability assay. LO2 cells were inoculated in 96-well plates and cultured with media containing Sor, Au-SS-PEG/Sor/ATP_{apt}, Au-SS-PEG/LM or Au-SS-PEG/Sor/ATP_{apt}/LM of different concentrations (0.01, 0.02, 0.03, and 0.04 μg mL^{-1}), with the drug-free medium as the control. After irradiation under 808 nm NIR light with a power density of 2 W cm^{-2} for 10 min, the cells were placed in a cell culture incubator for 24 h. Subsequently, the cells were washed with PBS and cultured with a fresh medium containing 10% CCK-8. Finally, the OD_{450} values were measured using a microplate reader (PerkinElmer, Austin, Texas, USA).

2.4.3 Apoptosis test. Cells were inoculated into 6-well plates and cultured with media containing the same concentration (0.04 μg mL^{-1}) of Sor, Au-SS-PEG/Sor/ATP_{apt}, or Au-SS-PEG/Sor/ATP_{apt}/LM medium for 6 h. After irradiation for 10 min under 808 nm NIR light with a power density of 2 W cm^{-2}, the cells were cultured for 24 h. Afterward, the cells were incubated with the working solution from an Annexin V-FITC/PI kit (BestBio, Shanghai, China) and were then collected for flow cytometry analysis.

2.4.4 Western blot analysis of PD-L1 expression. Proteins were extracted using lysis buffer (CST, USA), and the protein concentration was determined using the BCA assay. The protein samples were loaded onto 10% SDS-PAGE and separated by electrophoresis. After electrophoresis, the proteins were transferred onto a polyvinylidene difluoride membrane (Millipore, USA). The membrane was blocked with 5% skim milk at room temperature for 1 h to reduce nonspecific binding. It was then incubated overnight at 4 °C with anti-PD-L1 antibody (ab205921) and anti-β-actin antibody (ab8226). After washing, the membrane was incubated with a horseradish peroxidase (HRP)-conjugated secondary antibody (goat anti-rabbit IgG H&L, ab205718) at room temperature for 2 h. All antibodies were purchased from Abcam. Finally, protein bands were visualized using a chemiluminescence imaging system (Clinx, China) and enhanced chemiluminescence (ECL) reagent (Biosharp, China).

2.5 *In vivo* experiments

2.5.1 Establishment of tumor-bearing models. BALB/c-nude mice were obtained from Shanghai SLAC Laboratory Animal (Shanghai, China) and were housed in an animal facility with a 12-h light/dark cycle. These mice had unrestricted access to both water and food. For the xenograft assay, each mouse received a subcutaneous injection of 2×10^6 HepG2 cells into the right side of their back. All animal protocols were approved by the Animal Ethics Committee of Sir Run Run Shaw Hospital, Zhejiang University School of Medicine. Every procedure was carried out in strict accordance with relevant guidelines and regulations, including the principles for animal research outlined in the Guide for the Care and Use of Laboratory Animals (8th edition) published by the National Academies Press, USA.

 © 2025 The Author(s). Published by the Royal Society of Chemistry

Open Access Article. Published on 10 September 2025. Downloaded on 1/22/2026 1:25:36 PM. This article is licensed under a Creative Commons Attribution-NonCommercial 3.0 Unported Licence.

2.5.2 *In vivo* fluorescence imaging and drug distribution at the tumor site. To assess the distribution of the mentioned drugs in mice, tumor-bearing mice were randomly divided into three groups, each consisting of three mice. These groups received injections *via* the tail vein. The injections included the Au-SS-PEG/Sor/ATP_{apt} suspension, the Au-SS-PEG/Sor/ATP_{apt}/LM suspension, or PBS, all of which contained Cy5.5-NH_2. After a 36-h interval, real-time imaging was conducted by utilizing an *in vivo* imaging system (PerkinElmer, Austin, Texas, USA) from PerkinElmer in the USA.

To investigate the drug distribution at tumor sites, tumor-bearing mice treated with FITC-labeled Au-SS-PEG/Sor/ATP_{apt} or Au-SS-PEG/Sor/ATP_{apt}/LM were euthanized, and their tumors were dissected. The tumor samples underwent a series of processing steps, including fixation, dehydration, paraffin embedding, sectioning, dewaxing, rehydration, counterstaining with DAPI, mounting, and observation. Imaging was performed by utilizing an inverted fluorescence microscope from ZEISS (Göttingen, Germany).

2.5.3 *In vivo* thermal imaging. To evaluate the photothermal heating capability of the nanomaterials in mice, tumor-bearing mice were randomly divided into three groups ($n = 3$ per group). The injected formulations included the Au-SS-PEG/Sor/ATP_{apt}/LM suspension, an Au suspension or PBS (control). After intravenous tail vein injection, the tumor region was irradiated with an 808 nm NIR laser at 24 h post-injection. The temperature changes in the tumor area were monitored and recorded using an infrared thermal imaging camera.

2.5.4 *In vivo* anti-tumor and systemic toxicity evaluation. Fifteen tumor-bearing mice with initial tumor volumes ranging from 100–200 mm^3 were randomly divided into five groups, each consisting of three mice. These groups were denoted as follows: Group I (PBS), Group II (Sor), Group III (Au-SS-PEG/Sor), Group IV (Au-SS-PEG/Sor/ATP_{apt}), and Group V (Au-SS-PEG/Sor/ATP_{apt}/LM). Each group received injections at a dose of 2.5 mg kg^{-1} *via* the tail vein. After a 24-h interval, the mice underwent a 10-min irradiation with an 808 nm NIR light source at a power density of 2 W cm^{-2}. The injection and irradiation procedures were repeated once every five days. Tumor size was measured daily to generate tumor growth curves.

After the experiments, all surviving mice were euthanized, with their tumors dissected and fixed for subsequent histological analysis.

2.5.5 Establishment of the αPD-1-resistant mouse model. C57BL/6 mice were obtained from Shanghai SLAC Laboratory Animal in China and divided into two groups, each consisting of three mice. Subsequently, 5×10^5 cells per mL of H22 cells were subcutaneously injected into the right lower axilla of each mouse. Following 7 days, the experimental group received intraperitoneal injections of αPD-1 (0.1 mg g^{-1} body weight) for five consecutive days, while the control group received an equivalent volume of PBS. One week later, the injection procedure was repeated for another five days. After an additional week, a higher dose of αPD-1 (0.5 mg g^{-1} body weight) was administered intraperitoneally over the same duration. Tumors were then dissected and digested to obtain a single-cell suspension, which was subsequently reinjected into the mice. This process was repeated several times to establish the resistance index (RI) of tumor cells, which was determined through MTT assays (Fig. S4). The cells that exhibited resistance to αPD-1 treatment were then injected into the mice to establish the αPD-1-resistant mouse model.

2.5.6 Evaluating the anti-cancer effect of Au-SS-PEG/Sor/ATP_{apt}/LM in the αPD-1-resistant mouse model. C57BL/6 mice with αPD-1-resistant tumors were divided into four groups, each consisting of three mice. These groups were denoted as follows: Group I (PBS), Group II (αPD-1), Group III (Au-SS-PEG/Sor/ATP_{apt}/LM), and Group IV (Au-SS-PEG/Sor/ATP_{apt}/LM+αPD-1). An equal volume of the respective treatments was administered *via* intravenous injection. After a 24-h interval, all mice were exposed to 10 min of NIR irradiation. Five days later, mice in Group IV received simultaneous injections of Au-SS-PEG/Sor/ATP_{apt}/LM and αPD-1. Following 30 days of treatment, the surviving mice were euthanized, and their tumor tissues were dissected and photographed. A portion of the tissues was homogenized for ATP concentration measurement using an ATP detection kit (Beyotime Biotechnology, Shanghai, China), with readings taken with the use of a multi-functional microplate reader (PerkinElmer, Austin, Texas, USA). The remaining tissues were fixed for immunohistochemistry (IHC) assays, for which the following antibodies were used: anti-TGF-β (ab215715, Abcam, Cambridgeshire, UK) and anti-IL-10 (E-AB-70235, Elabscience, Houston, Texas, USA).

2.6 Statistical analysis

All experiments were conducted at least three independent times. The data were presented as mean ± standard deviation. Significance was measured by utilizing one-way ANOVA, Student's *t*-test, and the Newman–Keuls *post hoc* *t*-test, with GraphPad Prism 8.0 (USA) applied. $P < 0.05$ is considered significant (***$P < 0.001$, **$P < 0.01$, and *$P < 0.05$).

3 Results

3.1 Preparation and characterization of Au-SS-PEG/Sor/ATP_{apt}/LM nanoclusters

To confirm the composition of Au-SS-PEG/Sor/ATP_{apt}/LM nanoclusters prepared as described in Fig. 1(a), we conducted a series of experiments. We began by utilizing STEM to assess the size of Au-SH and Au-SS-PEG-COOH nanoclusters. The data indicated that Au-SH prepared using pipeline 1 exhibited a spherical shape with a uniform particle size of approximately 17 nm (Fig. S1(a and b)), while the size of Au-SH nanospheres prepared using pipeline 2 was around 8 nm (Fig. 1(b)). We proceeded with the preparation of Au-SS-PEG/Sor/ATP_{apt}/LM using pipeline 2 and observed the morphology of the resulting Au-SS-PEG-COOH and Au-SS-PEG/Sor/ATP_{apt}/LM nanoclusters. STEM analysis revealed that the sizes of these nanoclusters were approximately 8–10 nm and 50 nm, respectively (Fig. 1(c and d)). The zeta potentials of different nanomaterials during the preparation process are shown in Fig. S2. Consistent with these findings, DLS data verified that the size of Au-SH nanoparticles

Open Access Article. Published on 10 September 2025. Downloaded on 1/22/2026 1:25:36 PM.
This article is licensed under a Creative Commons Attribution-NonCommercial 3.0 Unported Licence.

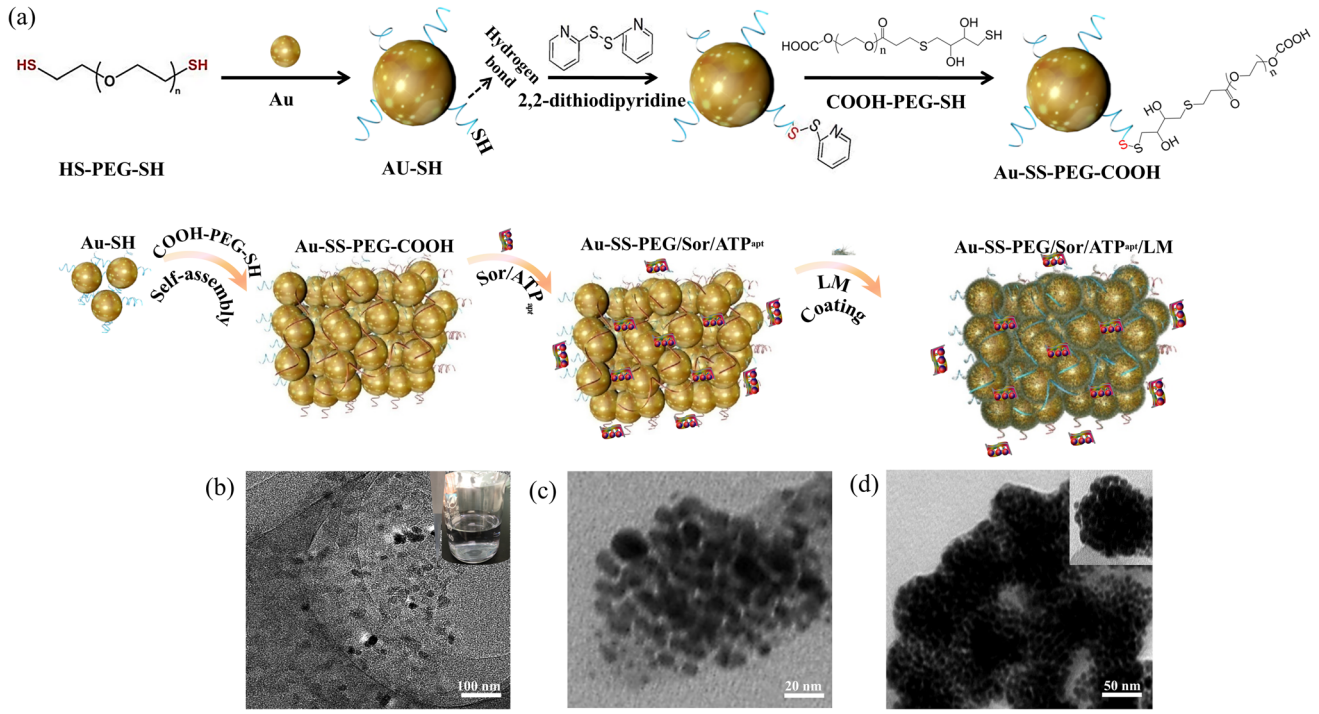

Fig. 1 Preparation and TEM images of Au-SS-PEG/Sor/ATP$_{apt}$/LM. (a) Schematic diagram of the preparation of Au-SS-PEG/Sor/ATP$_{apt}$/LM composite nanoclusters; (b) TEM image of Au-SH; (c) TEM image of Au-SS-PEG-COOH nanoclusters; (d) TEM image of Au-SS-PEG/Sor/ATP$_{apt}$/LM composite nanoclusters.

and Au-SS-PEG/Sor/ATP$_{apt}$/LM nanoclusters was roughly 8–10 nm and 50 nm, respectively (Fig. 2(a and b)).

Next, we carried out FTIR analysis to examine the functional groups on Au-SH and Au-SS-PEG nanoparticles. The outcomes indicated that the S–S stretching vibration of Au-SS-PEG peaked at 618 cm^{-1} in the spectrogram (Fig. 2(c)) and the C–O stretching vibration absorption peaked at 1380 cm^{-1} and 1250 cm^{-1}, confirming the successful synthesis of Au-SS-PEG. To validate the presence of Sor in these nanoclusters, we compared the UV absorption spectra of Sor and Au-SS-PEG/Sor/ATP$_{apt}$/LM. Both Sor and Au-SS-PEG/Sor/ATP$_{apt}$/LM exhibited distinct UV absorption near 260 nm (Fig. 2(d)). Subsequently, agarose gel electrophoresis was conducted to confirm the binding of ATP$_{apt}$ (27bp) to the Au-SS-PEG/Sor/ATP$_{apt}$ nanoclusters (Fig. 2(e)). Lastly, protein gel electrophoresis confirmed the presence of LM (4.6 kDa) in the Au-SS-PEG/Sor/ATP$_{apt}$/LM nanoclusters (Fig. 2(f)). Altogether, these results demonstrated the successful preparation of Au-SS-PEG/Sor/ATP$_{apt}$/LM nanoclusters.

3.2 Measurement of the performance of Au-SS-PEG/Sor/ATP$_{apt}$/LM nanoclusters

To assess the photothermal conversion efficiency of Au-SS-PEG/Sor/ATP$_{apt}$/LM nanoclusters, we subjected a suspension of these nanoclusters and PBS to NIR irradiation for 10 min. The thermal imaging data revealed that the temperature of the nanocluster suspension increased from 25 °C to 56.2 °C, while the temperature of PBS remained unchanged (Fig. 3(a)).

To explore the impact of Au-SS-PEG/Sor/ATP$_{apt}$/LM nanoclusters on blood cells, we conducted hemolysis tests using mouse blood. The results demonstrated that these nanoclusters did not induce hemolysis of mouse blood (Fig. 3(b)). Likewise, the erythrocytes in blood samples incubated with various concentrations of Au-SS-PEG/Sor/ATP$_{apt}$/LM remained intact (Fig. 3(c)). TEM findings indicated that these nanoclusters were not internalized by erythrocytes and the erythrocyte cell membranes appeared smooth and intact, with no observable hemoglobin leakage (Fig. 3(d)). Additionally, we incubated the nanoclusters with FBS to evaluate their interaction with macromolecules in plasma. Both protein gel electrophoresis and DLS data revealed that these nanoclusters did not adsorb plasma proteins, and their size did not dramatically change after 24 h of incubation with FBS (Fig. 3(e and f)).

We established the standard curve of Sor (Fig. S3) using UV-Vis spectrophotometry and calculated the encapsulation efficiency and drug loading capacity of Au-SS-PEG for Sor to be 71.2% and 4.7%, respectively, according to the formula. To test the release of Sor loaded in the Au-SS-PEG/Sor/ATP$_{apt}$/LM nanoclusters, we measured the concentration of free Sor in response to GSH and/or ATP treatment. The results manifested that either GSH or ATP significantly boosted the release of Sor, with a more pronounced effect observed in the presence of both GSH and ATP (Fig. 3(g)). Taken together, these findings demonstrated that Au-SS-PEG/Sor/ATP$_{apt}$/LM nanoclusters exhibit excellent photothermal conversion performance, high blood compatibility, and efficient Sor release in response to GSH/ATP.

 © 2025 The Author(s). Published by the Royal Society of Chemistry

Open Access Article. Published on 10 September 2025. Downloaded on 1/22/2026 1:25:36 PM.
This article is licensed under a Creative Commons Attribution-NonCommercial 3.0 Unported Licence.

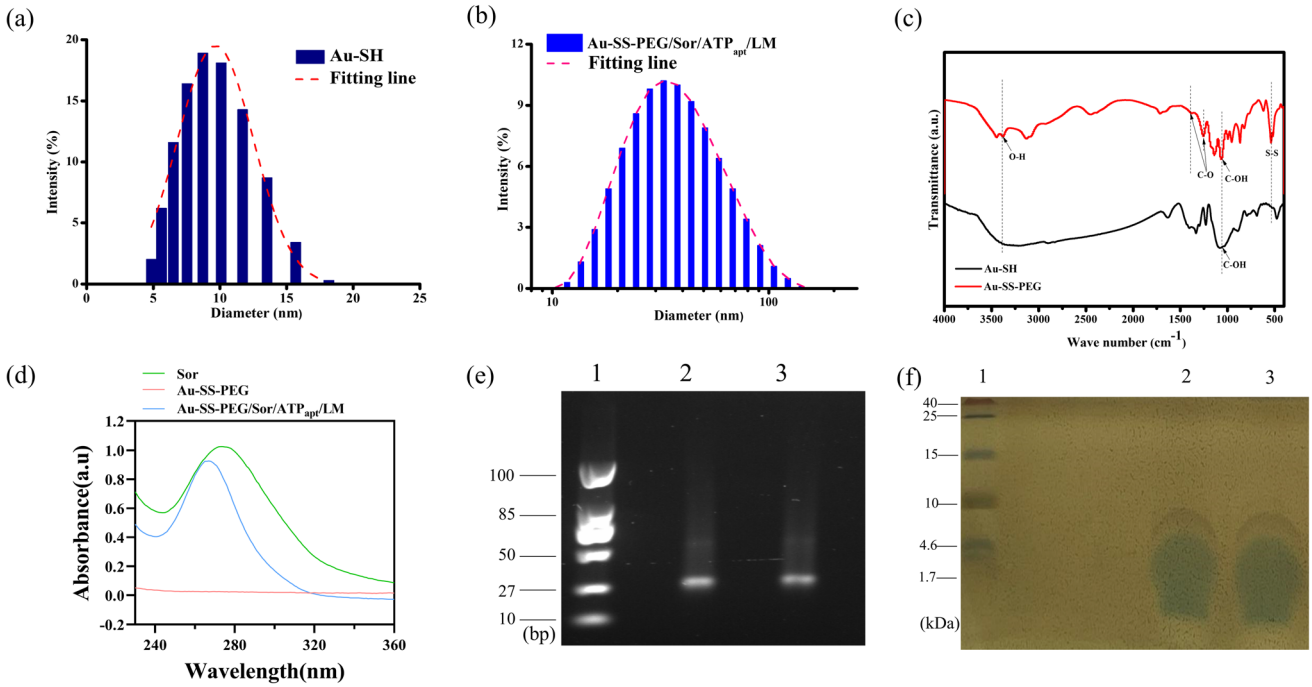

Fig. 2 Characterization of Au-SS-PEG/Sor/ATPapt/LM (a and b) DLS results showing the particle size distribution of Au-SH (a) and Au-SS-PEG/Sor/ATP$_{apt}$/LM composite nanoclusters (b); (c) infrared spectra of Au-SH and Au-SS-PEG; (d) UV absorption spectra of Sor and Au-SS-PEG/Sor/ATP$_{apt}$/LM; (e) DNA gel electrophoresis data confirming ATP$_{apt}$ presence in Au-SS-PEG/Sor/ATP$_{apt}$ nanoclusters (lane 3) (lane 1: marker; lane 2: ATP$_{apt}$; lane 3: Au-SS-PEG/Sor/ATP$_{apt}$); (f) protein gel electrophoresis data indicating coating of LM (4.6 kDa) on the Au-SS-PEG/Sor/ATP$_{apt}$/LM nanoclusters (lane 1: marker; lane 2: LM; lane 3: Au-SS-PEG/Sor/ATP$_{apt}$/LM).

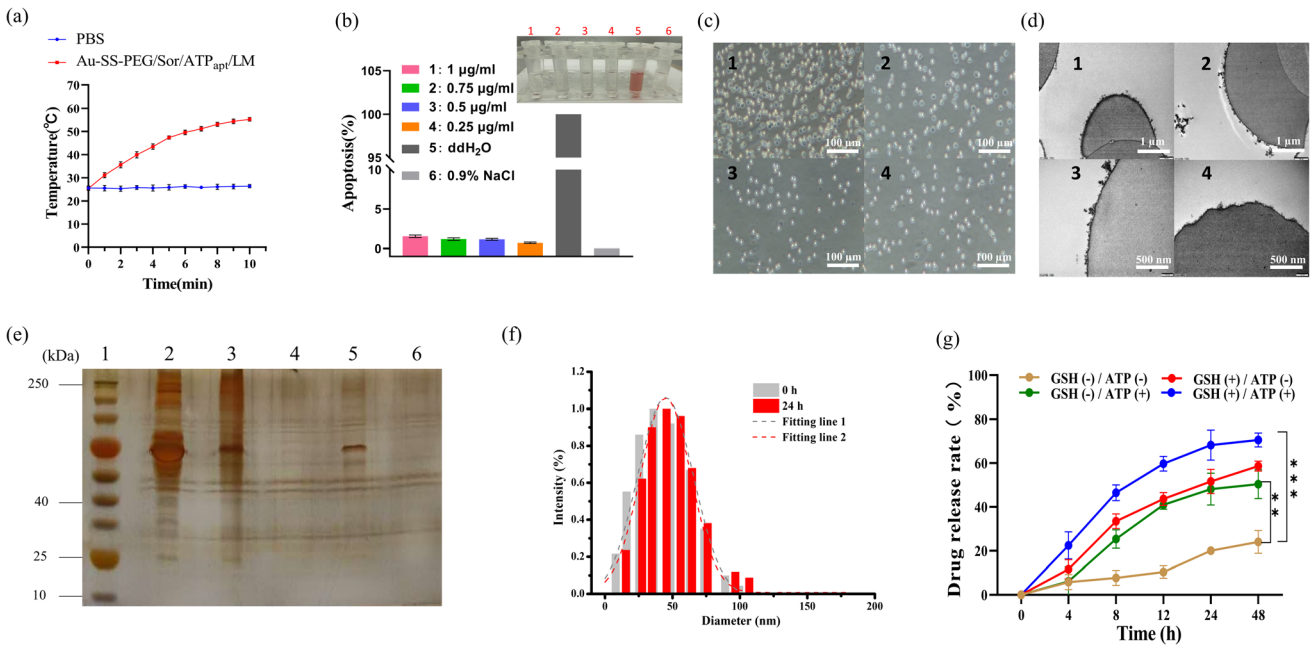

Fig. 3 Measurement of Au-SS-PEG/Sor/ATP$_{apt}$/LM performance. (a) Curves showing the temperature change of the Au-SS-PEG/Sor/ATP$_{apt}$/LM suspension and PBS upon NIR treatment; (b) effects of Au-SS-PEG/Sor/ATP$_{apt}$/LM nanoclusters on the hemolysis of mouse erythrocytes; (c and d) bright-field image (c) and TEM image (d) of mouse erythrocytes in samples #1–4 shown in (b); (e) protein gel electrophoresis results depicting the binding of FBS proteins to the indicated nanoclusters. Lane 2 (FBS), lane 3 (Au), lane 4 (AU-SH), lane 5 (Au-SS-PEG), and lane 6 (Au-SS-PEG/Sor/ATP$_{apt}$/LM); (f) DLS data indicating the size change of Au-SS-PEG/Sor/ATP$_{apt}$/LM nanoclusters before and after incubation (0 h and 24 h) with FBS; (g) the concentration of released Sor over time from Au-SS-PEG/Sor/ATP$_{apt}$/LM upon the indicated treatments.

Open Access Article. Published on 10 September 2025. Downloaded on 1/22/2026 1:25:36 PM.
This article is licensed under a Creative Commons Attribution-NonCommercial 3.0 Unported Licence.

3.3 The anti-cancer effect of Au-SS-PEG/Sor/ATP$_{apt}$/LM nanoclusters *in vitro*

To investigate the anti-cancer effect of Au-SS-PEG/Sor/ATPapt/LM nanoclusters on HCC, we initially assessed the uptake of FITC-labeled nanoclusters by LO2 hepatocytes and HepG2 HCC cells. Confocal microscopy data revealed that LO2 cells did not absorb Au-SS-PEG/Sor/ATP$_{apt}$/LM nanoclusters, and only a small amount of Au-SS-PEG/Sor/ATP$_{apt}$ nanoclusters were taken up by HepG2 cells. However, the LM coating significantly facilitated the absorption of Au-SS-PEG/Sor/ATP$_{apt}$ nanoclusters by HepG2 cells (Fig. 4(a)). We then evaluated the cytotoxicity of these nanoclusters to LO2 cells by employing a CCK-8 staining assay. The results indicated that the viability of LO2 cells treated with Au-SS-PEG/Sor/ATP$_{apt}$ or Au-SS-PEG/Sor/ATP$_{apt}$/LM was not reduced compared to cells treated with Sor, as shown by the CCK-8 assay results (Fig. 4(b)).

Next, we conducted Annexin V/PI staining assays to assess the apoptosis of HepG2 cells treated with PBS, Sor, Au-SS-PEG/Sor/ATP$_{apt}$, or Au-SS-PEG/Sor/ATP$_{apt}$/LM. The findings suggested that SS-PEG/Sor/ATP$_{apt}$/LM remarkably enhanced the pro-apoptotic effect of Sor or SS-PEG/Sor/ATP$_{apt}$ in HepG2 cells (Fig. 4(c and d)). These results collectively indicated that SS-PEG/Sor/ATP$_{apt}$/LM can intensify the anti-cancer effect of Sor in HCC cells without heightening the cytotoxicity to normal hepatocytes. Finally, we examined PD-L1 expression on HepG2 cell surfaces through western blot analysis. As shown in Fig. 4(e), the Au-SS-PEG/Sor/ATP$_{apt}$/LM group demonstrated the most significant reduction in PD-L1 expression, thereby effectively enhancing immunotherapy efficacy.

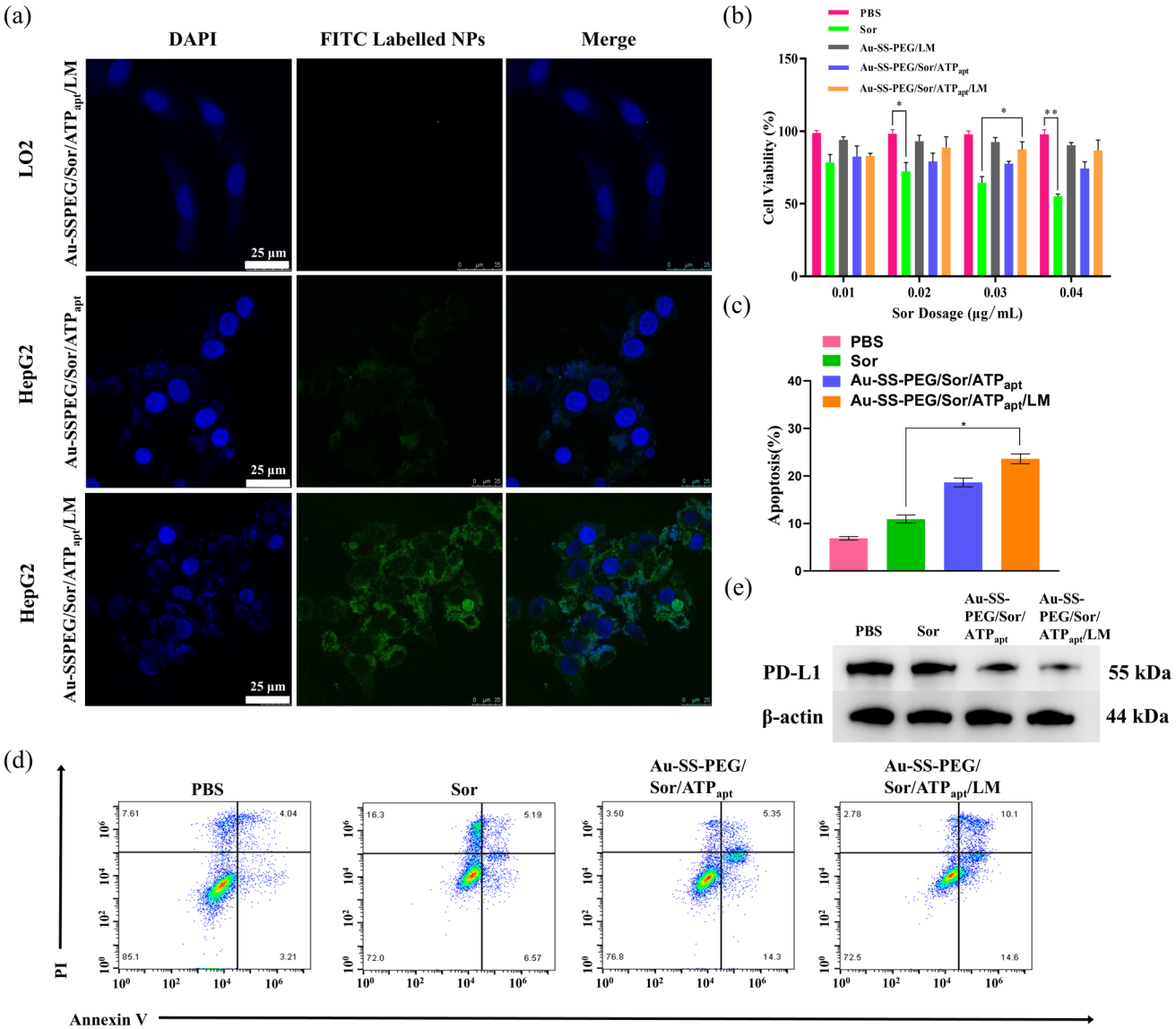

Fig. 4 Cytotoxic effect of released Sor from Au-SS-PEG/Sor/ATP$_{apt}$/LM. (a) Confocal images of LO2 and HepG2 incubated with the indicated nanoclusters; (b) CCK-8 assay data showing the viability of LO2 cells with the indicated treatments; (c and d) Annexin V/PI staining results depicting the apoptosis of HepG2 cells with the indicated treatments; (e) western blot analysis of PD-L1 expression in HepG2 cells under different treatments.

 © 2025 The Author(s). Published by the Royal Society of Chemistry

Open Access Article. Published on 10 September 2025. Downloaded on 1/22/2026 1:25:36 PM.
This article is licensed under a Creative Commons Attribution-NonCommercial 3.0 Unported Licence.

3.4 The anti-cancer effect of Au-SS-PEG/Sor/ATP$_{apt}$/LM nanoclusters in HCC xenograft mice

To evaluate the anti-cancer effect of Au-SS-PEG/Sor/ATP$_{apt}$/LM nanoclusters *in vivo*, we established an HCC xenograft mouse model and injected cy5.5-labeled nanoclusters into these mice. Using *in vivo* imaging and fluorescence microscopy, we observed that the fluorescent signal in the xenograft tumors of mice injected with Au-SS-PEG/Sor/ATP$_{apt}$/LM was significantly stronger than that in mice injected with Au-SS-PEG/Sor/ATP$_{apt}$ or PBS (Fig. 5(a–c)). To evaluate the photothermal performance of nanomaterials *in vivo*, we intravenously administered different nanoparticle formulations *via* tail vein injection. At 24 h post-injection, the tumor region was irradiated with an NIR laser while monitoring temperature changes using infrared thermal imaging. As demonstrated in Fig. 5(d and e), the Au-SS-PEG/Sor/ATP$_{apt}$/LM group exhibited the most significant tumor accumulation, consequently achieving the highest temperature elevation up to 54.7 °C upon laser irradiation. We then measured the size and volume of xenograft tumors dissected from the mice receiving different treatments, while simultaneously monitoring changes in body weight. The results showed that Sor-treated tumors were notably smaller than PBS-treated tumors. Tumors treated with Au-SS-PEG/Sor or Au-SS-PEG/Sor/ATP$_{apt}$ had similar sizes, which were smaller than Sor-treated tumors. Tumors treated with Au-SS-PEG/Sor/ATP$_{apt}$/LM were the smallest (Fig. 5(f and g)). No significant abnormal changes in body weight were observed in the mice during the entire treatment period (Fig. 5(h)). H&E staining data confirmed a significant reduction in tumor cell density within the xenograft tumors treated with Au-SS-PEG/Sor/ATP$_{apt}$/LM compared to tumors in the other treatment groups (Fig. 5(i)). These results indicated that Au-SS-PEG/Sor/ATP$_{apt}$/LM effectively targets HCC cells and suppresses their growth *in vivo*.

3.5 The impact of Au-SS-PEG/Sor/ATP$_{apt}$/LM on αPD-1-resistant HCC mice

To determine the anti-cancer effect of Au-SS-PEG/Sor/ATPapt/LM nanoclusters in an immunotherapy drug-resistant HCC model *in vivo*, we established an αPD-1-resistant HCC mouse model. After 30 days of treatment, the size of tumors from PBS- and αPD-1-treated mice was similar, confirming the resistance of these tumors to αPD-1 therapy. However, the tumors from mice treated with Au-SS-PEG/Sor/ATP$_{apt}$/LM or Au-SS-PEG/Sor/ATP$_{apt}$/LM+αPD-1 exhibited pronounced shrinkage (Fig. 6(a)). Since αPD-1-resistant tumors have elevated levels of extracellular ATP/ADO and immunosuppressive factors such as IL-10 and TGF-β,[34] we tested the ATP concentration and the expression of IL-10 and TGF-β within the tumors. The results indicated that tumors from mice treated with Au-SS-PEG/Sor/ATP$_{apt}$/LM or Au-SS-PEG/Sor/ATP$_{apt}$/LM+αPD-1 exhibited a substantial reduction in the ATP concentration and IL-10/TGF-β expression compared to tumors treated with PBS or αPD-1 (Fig. 6(b and c)). Finally, the infiltration of CD3$^+$ CD69$^+$ T cells into tumor tissues of mice was analyzed by flow cytometry. As shown in Fig. 6(d), the Au-SS-PEG/Sor/ATP$_{apt}$/LM+αPD-1 group exhibited the highest T cell infiltration at 14.06%, surpassing all other groups. These findings demonstrated that Au-SS-PEG/Sor/ATP$_{apt}$/LM nanoclusters alone are sufficient to hinder the growth of αPD-1-resistant HCC tumors.

4 Discussion

While novel therapies like immune checkpoint inhibitors have dramatically improved the prognosis of HCC patients, HCC remains one of the deadliest cancers globally due to factors such as drug resistance and lack of more effective drug delivery methods.[35]

The development of nanodrug delivery systems has the potential to enhance the stability, biocompatibility, permeability, and retention of anti-cancer drugs,[36] ultimately improving the survival rates of cancer patients. In this project, a novel nanodrug delivery system was set up to achieve a stepwise release of anti-cancer drugs in response to the high levels of GSH and ATP/ADO in HCC cells.

Various biomaterials, including polymers, liposomes, and metal nanoparticles, have been explored for delivering anti-cancer drugs. Notably, nanoparticles have been extensively studied as carriers for improving the targeting and therapeutic effects of Sor, a drug with limitations such as rapid metabolism, poor solubility, and low bioavailability, which hinder its efficacy in treating HCC.[37] For instance, Babos *et al.*[38] employed PEG and PEG-PLGA polymer nanoparticles to encapsulate doxorubicin and Sor, achieving a controlled release of these drugs. Tahir *et al.*[39] prepared lipid polymer hybrid nanoparticles loaded with Sor using bulk nanoprecipitation, microfluidic forward flow, and nano-precipitation techniques and demonstrated their stability, biocompatibility, and safety in biological media.

In contrast, the system developed in this project leverages the high concentrations of GSH and ATP/ADO in cancer cells and the TME, reducing the uncontrolled release of Sor in non-cancerous tissues. Additionally, the system includes ATP$_{apt}$, which can aid in reducing the ATP/ADO levels in the TME, thus mitigating their contribution to drug resistance. The LM coating further enhances the targeted delivery of Sor into HCC, bolstering its anti-cancer effect. This approach could potentially be applied to the delivery of drugs for treating other cancers expressing LHRH receptors, such as breast, ovarian, and prostate cancers. Indeed, Tang *et al.*[40] pointed out that in LHRH receptor-expressing MCF-7 breast cancer cells, the LHRH peptide enhances DNA internalization and reduces cytotoxicity. It would be interesting to determine whether LM coating has a similar effect in other cancers expressing LHRH receptors.

Importantly, the Au-SS-PEG/Sor/ATPapt/LM nanoclusters demonstrated a great anti-cancer effect in αPD-1-resistant HCC tumors. This effect is likely achieved through improved targeted delivery of Sor, increasing its absorption and utilization efficiency, rather than resensitizing αPD-1-resistant HCC cells to αPD-1 drugs. Alternatively, ATP$_{apt}$ could also contribute to overcoming drug resistance, as the high level of ATP/ADO triggers the development of drug resistance.[41–44] Further investigation is warranted to determine the precise mechanism by which

Open Access Article. Published on 10 September 2025. Downloaded on 1/22/2026 1:25:36 PM.
This article is licensed under a Creative Commons Attribution-NonCommercial 3.0 Unported Licence.

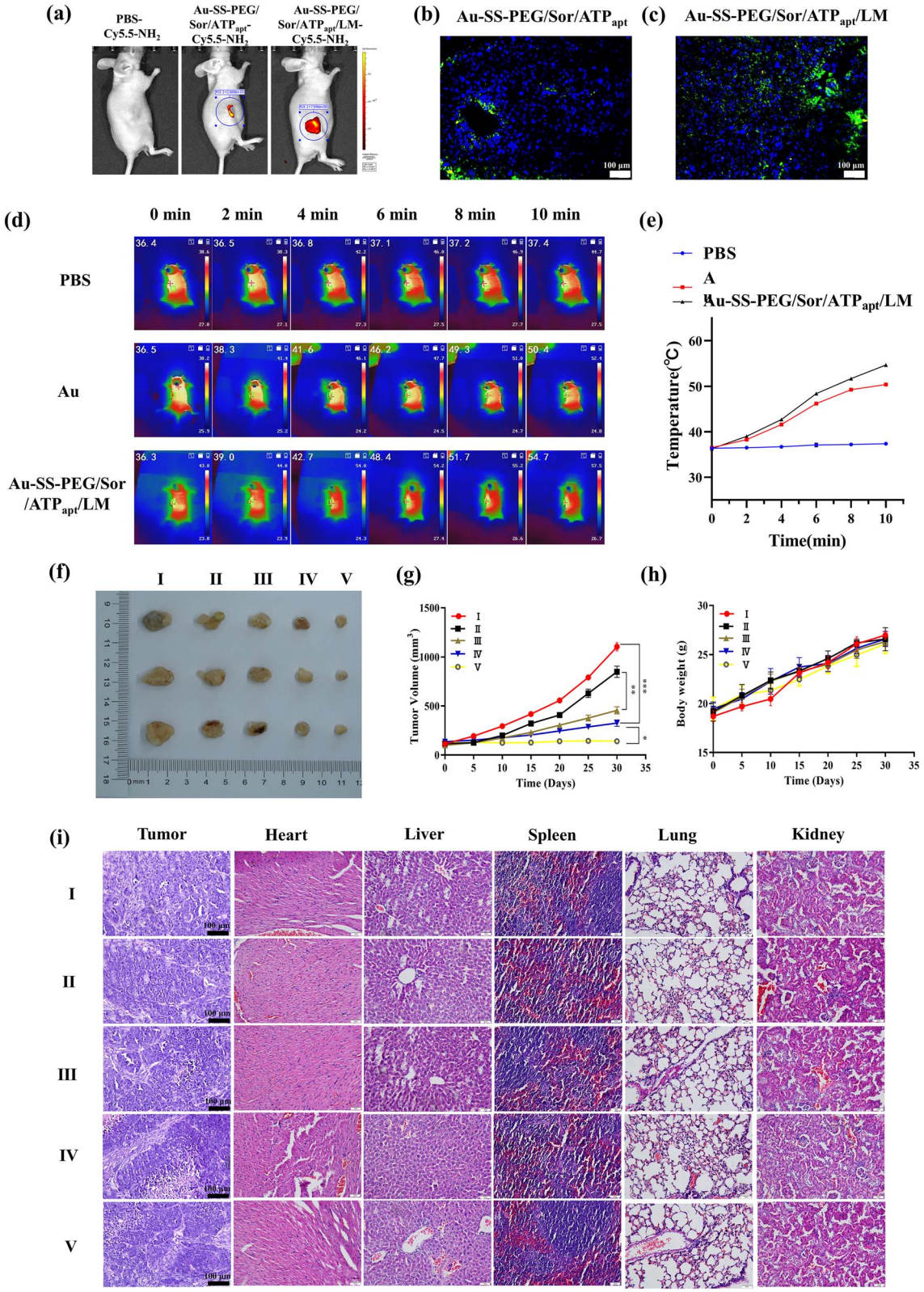

Fig. 5 Anti-cancer effect of Au-SS-PEG/Sor/ATP_{apt}/LM in HCC xenograft mice. (a) Fluorescence distribution of the indicated nanoclusters in HCC xenograft mice (36 h after injection); (b and c) fluorescence distribution of the indicated FITC-labeled nanoclusters in xenograft tumors; (d) *in vivo* thermal imaging of mice; (e) temperature elevation curves in mice; (f) the morphology of xenograft tumors dissected from mice injected with PBS (I), Sor (II), Au-SS-PEG/Sor (III), Au-SS-PEG/Sor/ATP_{apt} (IV), and Au-SS-PEG/Sor/ATP_{apt}/LM (V); (g) curves showing the volume change of tumors from mice assayed in (f); (h) body weight changes of mice during the treatment period; (i) H&E results of the xenograft tumors from mice assayed in (f).

 © 2025 The Author(s). Published by the Royal Society of Chemistry

Open Access Article. Published on 10 September 2025. Downloaded on 1/22/2026 1:25:36 PM.
This article is licensed under a Creative Commons Attribution-NonCommercial 3.0 Unported Licence.

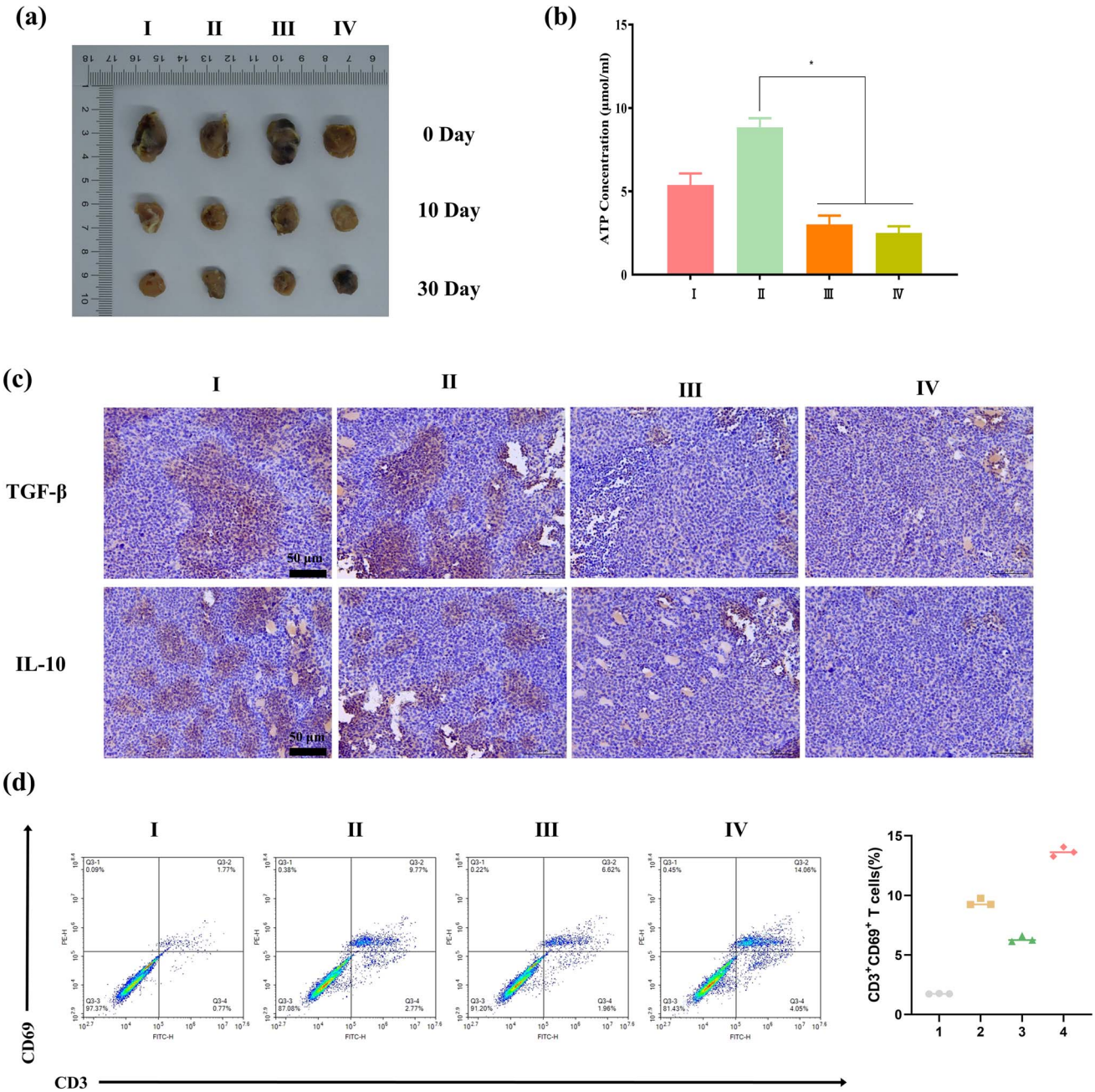

Fig. 6 Anti-cancer effect of Au-SS-PEG/Sor/ATP_{apt}/LM in αPD-1-resistant mice. (a) The morphology of tumors from mice treated with PBS (I), αPD-1 (II), Au-SS-PEG/Sor/ATP_{apt}/LM (III), and Au-SS-PEG/Sor/ATP_{apt}/LM+αPD-1 (IV) at the indicated time points; (b) ATP concentration in tumor tissues from mice with the indicated treatments in (a); (c) IHC data showing the expression of TGF-β and IL-10 in tumor tissues from mice with the indicated treatments in (a); (d) flow cytometry analysis of $CD3^+$ $CD69^+$ T cell infiltration in mouse tumor tissues.

our nanoclusters repress the growth of αPD-1-resistant HCC tumors.

In conclusion, the novel nanodrug delivery system developed in this project manifested promise for enhancing the efficiency of targeted Sor delivery in HCC and exhibits excellent biocompatibility and anti-cancer effects. This system holds great potential for HCC treatments, particularly for αPD-1-resistant patients.

Ethical statement

All animal protocols were approved by the Animal Ethics Committee of Sir Run Run Shaw Hospital, Zhejiang University School of Medicine. Every procedure was carried out in strict accordance with relevant guidelines and regulations, including the principles for animal research outlined in the Guide for the Care and Use of Laboratory Animals (8th edition) published by the National Academies Press, USA.

Open Access Article. Published on 10 September 2025. Downloaded on 1/22/2026 1:25:36 PM.
This article is licensed under a Creative Commons Attribution-NonCommercial 3.0 Unported Licence.

Conflicts of interest

The authors have declared that no competing interest exists.

Data availability

Data will be made available on reasonable request.

Supplementary information is available. See DOI: https://doi.org/10.1039/d5na00056d.

Acknowledgements

The Youth Foundation of Natural Science Foundation of Xinjiang Uygur Autonomous Region (2021D01C241) and Chinese Society of Clinical Oncology (CSCO) Oncology Research Foundation (Grant No. Y-Roche2019/2-0042) are acknowledged.

References

1 K. A. McGlynn, J. L. Petrick and H. B. El-Serag, Epidemiology of Hepatocellular Carcinoma, *Hepatology*, 2021, **73**(Suppl 1), 4–13, DOI: 10.1002/hep.31288.

2 C. Donisi, M. Puzzoni, P. Ziranu, *et al.*, Immune Checkpoint Inhibitors in the Treatment of HCC, *Front. Oncol.*, 2020, **10**, 601240, DOI: 10.3389/fonc.2020.601240.

3 R. S. Finn, B. Y. Ryoo, P. Merle, *et al.*, Pembrolizumab As Second-Line Therapy in Patients With Advanced Hepatocellular Carcinoma in KEYNOTE-240: A Randomized, Double-Blind, Phase III Trial, *J. Clin. Oncol.*, 2020, **38**, 193–202, DOI: 10.1200/JCO.19.01307.

4 J. J. G. Marin, R. I. R. Macias, M. J. Monte, *et al.*, Molecular Bases of Drug Resistance in Hepatocellular Carcinoma, *Cancers*, 2020, **12**, 1663, DOI: 10.3390/cancers12061663.

5 R. J. Honeywell, C. Fatmawati, M. Boeddha, *et al.*, Abstract 3785: Human pharmacokinetics (PK) of selected tyrosine kinase inhibitors (TKI) in relation to transport characteristics in a polarized gut epithelium model system, *Cancer Res.*, 2012, **72**, 3785, DOI: 10.1158/1538-7445.AM2012-3785.

6 B. Allard, M. S. Longhi, S. C. Robson, *et al.*, The ectonucleotidases CD39 and CD73: Novel checkpoint inhibitor targets, *Immunol. Rev.*, 2017, **276**, 121–144, DOI: 10.1111/imr.12528.

7 R. D. Leone and L. A. Emens, Targeting adenosine for cancer immunotherapy, *J. ImmunoTher. Cancer*, 2018, **6**, 57, DOI: 10.1186/s40425-018-0360-8.

8 D. J. Chiang, S. Roychowdhury, K. Bush, *et al.*, Adenosine 2A receptor antagonist prevented and reversed liver fibrosis in a mouse model of ethanol-exacerbated liver fibrosis, *PLoS One*, 2013, **8**, e69114, DOI: 10.1371/journal.pone.0069114.

9 A. Badimon, H. J. Strasburger, P. Ayata, *et al.*, Negative feedback control of neuronal activity by microglia, *Nature*, 2020, **586**, 417–423, DOI: 10.1038/s41586-020-2777-8.

10 A. K. Moesta, X. Y. Li and M. J. Smyth, Targeting CD39 in cancer, *Nat. Rev. Immunol.*, 2020, **20**, 739–755, DOI: 10.1038/s41577-020-0376-4.

11 J. Linden, F. Koch-Nolte and G. Dahl, Purine Release, Metabolism, and Signaling in the Inflammatory Response, *Annu. Rev. Immunol.*, 2019, **37**, 325–347, DOI: 10.1146/annurev-immunol-051116-052406.

12 V. V. Veselov, A. E. Nosyrev, L. Jicsinszky, *et al.*, Targeted Delivery Methods for Anticancer Drugs, *Cancers*, 2022, **14**, 622, DOI: 10.3390/cancers14030622.

13 S. Senapati, A. K. Mahanta, S. Kumar, *et al.*, Controlled drug delivery vehicles for cancer treatment and their performance, *Signal Transduction Targeted Ther.*, 2018, **3**, 7, DOI: 10.1038/s41392-017-0004-3.

14 R. Wang, Q. Shen, X. Li, *et al.*, Efficacy of inverso isomer of CendR peptide on tumor tissue penetration, *Acta Pharm. Sin. B*, 2018, **8**, 825–832, DOI: 10.1016/j.apsb.2018.06.006.

15 A. Gabizon, H. Shmeeda and Y. Barenholz, Pharmacokinetics of pegylated liposomal Doxorubicin: review of animal and human studies, *Clin. Pharmacokinet.*, 2003, **42**, 419–436, DOI: 10.2165/00003088-200342050-00002.

16 S. S. Dharap, B. Qiu, G. C. Williams, *et al.*, Molecular targeting of drug delivery systems to ovarian cancer by BH3 and LHRH peptides, *J. Controlled Release*, 2003, **91**, 61–73, DOI: 10.1016/s0168-3659(03)00209-8.

17 X. Li, O. Taratula, O. Taratula, *et al.*, LHRH-Targeted Drug Delivery Systems for Cancer Therapy, *Mini-Rev. Med. Chem.*, 2017, **17**, 258–267, DOI: 10.2174/1389557516666161013111155.

18 H. Yin, K. W. Cheng, H. L. Hwa, *et al.*, Expression of the messenger RNA for gonadotropin-releasing hormone and its receptor in human cancer cell lines, *Life Sci.*, 1998, **62**, 2015–2023, DOI: 10.1016/s0024-3205(98)00173-8.

19 K. Szepeshazi, A. V. Schally, A. Treszl, *et al.*, Therapy of experimental hepatic cancers with cytotoxic peptide analogs targeted to receptors for luteinizing hormone-releasing hormone, somatostatin or bombesin, *Anticancer Drugs*, 2008, **19**, 349–358, DOI: 10.1097/CAD.0b013e3282f9adce.

20 X. Liu, L. Zhu, J. Ma, *et al.*, Target-specific delivery of siRNA into hepatoma cells' cytoplasm by bifunctional carrier peptide, *Drug Delivery Transl. Res.*, 2017, **7**, 147–155, DOI: 10.1007/s13346-016-0348-1.

21 L. Liu, X. Dong, D. Zhu, *et al.*, TAT-LHRH conjugated low molecular weight chitosan as a gene carrier specific for hepatocellular carcinoma cells, *Int. J. Nanomed.*, 2014, **9**, 2879–2889, DOI: 10.2147/IJN.S61392.

22 L. Liu, H. Wang, Q. Liu, *et al.*, Biodistribution of TAT-LHRH conjugated chitosan/DNA nanoparticles in the mice bearing hepatoma xenografts, *J. Biomed. Mater. Res.*, 2016, **104**, 2394–2400, DOI: 10.1002/jbm.a.35775.

23 E. K. Manesis, G. Giannoulis, P. Zoumboulis, *et al.*, Treatment of hepatocellular carcinoma with combined suppression and inhibition of sex hormones: a randomized, controlled trial, *Hepatology*, 1995, **21**, 1535–1542.

24 E. V. Kalinina and L. A. Gavriliuk, Glutathione Synthesis in Cancer Cells, *Biochemistry*, 2020, **85**, 895–907, DOI: 10.1134/S0006297920080052.

 © 2025 The Author(s). Published by the Royal Society of Chemistry

Open Access Article. Published on 10 September 2025. Downloaded on 1/22/2026 1:25:36 PM.
This article is licensed under a Creative Commons Attribution-NonCommercial 3.0 Unported Licence.

25 H. Tang, D. Chen, C. Li, *et al.*, Dual GSH-exhausting sorafenib loaded manganese-silica nanodrugs for inducing the ferroptosis of hepatocellular carcinoma cells, *Int. J. Pharm.*, 2019, **572**, 118782, DOI: 10.1016/j.ijpharm.2019.118782.
26 G. Yang, C. Chen, Y. Zhu, *et al.*, GSH-Activatable NIR Nanoplatform with Mitochondria Targeting for Enhancing Tumor-Specific Therapy, *ACS Appl. Mater. Interfaces*, 2019, **11**, 44961–44969, DOI: 10.1021/acsami.9b15996.
27 N. Yan, L. Lin, C. Xu, *et al.*, A GSH-Gated DNA Nanodevice for Tumor-Specific Signal Amplification of microRNA and MR Imaging-Guided Theranostics, *Small*, 2019, **15**, e1903016, DOI: 10.1002/smll.201903016.
28 E. H. Jeong, G. Jung, C. A. Hong, *et al.*, Gold nanoparticle (AuNP)-based drug delivery and molecular imaging for biomedical applications, *Arch. Pharmacal Res.*, 2014, **37**, 53–59, DOI: 10.1007/s12272-013-0273-5.
29 S. Lee, G. Hwang, T. H. Kim, *et al.*, On-Demand Drug Release from Gold Nanoturf for a Thermo- and Chemotherapeutic Esophageal Stent, *ACS Nano*, 2018, **12**, 6756–6766, DOI: 10.1021/acsnano.8b01921.
30 T. Wang, J. F. Fahrmann, H. Lee, *et al.*, JAK/STAT3-Regulated Fatty Acid beta-Oxidation Is Critical for Breast Cancer Stem Cell Self-Renewal and Chemoresistance, *Cell Metab.*, 2018, **27**, 136–150e135, DOI: 10.1016/j.cmet.2017.11.001.
31 J. Zhao, Y. Yang, X. Han, *et al.*, Redox-Sensitive Nanoscale Coordination Polymers for Drug Delivery and Cancer Theranostics, *ACS Appl. Mater. Interfaces*, 2017, **9**, 23555–23563, DOI: 10.1021/acsami.7b07535.
32 Q. Feng, Y. Shen, Y. Fu, *et al.*, Self-Assembly of Gold Nanoparticles Shows Microenvironment-Mediated Dynamic Switching and Enhanced Brain Tumor Targeting, *Theranostics*, 2017, **7**, 1875–1889, DOI: 10.7150/thno.18985.
33 Q. Zhao, Y. Yang, H. Wang, *et al.*, Gold nanoparticles modified hollow carbon system for dual-responsive release and chemo-photothermal synergistic therapy of tumor, *J. Colloid Interface Sci.*, 2019, **554**, 239–249, DOI: 10.1016/j.jcis.2019.07.005.
34 Q. Lei, D. Wang, K. Sun, *et al.*, Resistance Mechanisms of Anti-PD1/PDL1 Therapy in Solid Tumors, *Front. Cell Dev. Biol.*, 2020, **8**, 672, DOI: 10.3389/fcell.2020.00672.
35 S. Yang, C. Cai, H. Wang, *et al.*, Drug delivery strategy in hepatocellular carcinoma therapy, *Cell Commun. Signaling*, 2022, **20**, 26, DOI: 10.1186/s12964-021-00796-x.
36 Y. Yao, Y. Zhou, L. Liu, *et al.*, Nanoparticle-Based Drug Delivery in Cancer Therapy and Its Role in Overcoming Drug Resistance, *Front. Mol. Biosci.*, 2020, **7**, 193, DOI: 10.3389/fmolb.2020.00193.
37 F. H. Kong, Q. F. Ye, X. Y. Miao, *et al.*, Current status of sorafenib nanoparticle delivery systems in the treatment of hepatocellular carcinoma, *Theranostics*, 2021, **11**, 5464–5490, DOI: 10.7150/thno.54822.
38 G. Babos, E. Biro, M. Meiczinger, *et al.*, Dual Drug Delivery of Sorafenib and Doxorubicin from PLGA and PEG-PLGA Polymeric Nanoparticles, *Polymers*, 2018, **10**, 895, DOI: 10.3390/polym10080895.
39 N. Tahir, A. Madni, W. Li, *et al.*, Microfluidic fabrication and characterization of Sorafenib-loaded lipid-polymer hybrid nanoparticles for controlled drug delivery, *Int. J. Pharm.*, 2020, **581**, 119275, DOI: 10.1016/j.ijpharm.2020.119275.
40 Q. Tang, B. Cao, H. Wu, *et al.*, Selective gene delivery to cancer cells using an integrated cationic amphiphilic peptide, *Langmuir*, 2012, **28**, 16126–16132, DOI: 10.1021/la303299s.
41 M. Paskeviciute and V. Petrikaite, Overcoming transporter-mediated multidrug resistance in cancer: failures and achievements of the last decades, *Drug Delivery Transl. Res.*, 2019, **9**, 379–393, DOI: 10.1007/s13346-018-0584-7.
42 H. Wang, Z. Gao, X. Liu, *et al.*, Targeted production of reactive oxygen species in mitochondria to overcome cancer drug resistance, *Nat. Commun.*, 2018, **9**, 562, DOI: 10.1038/s41467-018-02915-8.
43 P. J. Schuler, Z. Saze, C. S. Hong, *et al.*, Human CD4+ CD39+ regulatory T cells produce adenosine upon co-expression of surface CD73 or contact with CD73+ exosomes or CD73+ cells, *Clin. Exp. Immunol.*, 2014, **177**, 531–543, DOI: 10.1111/cei.12354.
44 P. Vaupel and G. Multhoff, Adenosine can thwart antitumor immune responses elicited by radiotherapy : Therapeutic strategies alleviating protumor ADO activities, *Strahlenther. Onkol.*, 2016, **192**, 279–287, DOI: 10.1007/s00066-016-0948-1.